Structural modifications and thermal stability of Cd2+ -exchanged stellerite, a zeolite with STI framework-type

Cametti, G.; Scheinost, A. C.; Churakov, S. V.;

Originally published:

September 2019

Journal of Physical Chemistry C 123(2019), 25236-25245

DOI: https://doi.org/10.1021/acs.jpcc.9b07297

Structural modifications and thermal stability of Cd^{2+} -exchanged stellerite, a zeolite with STI framework-type

G. Cametti,[*,†] A. C. Scheinost,[‡,¶] and S. V. Churakov[†,§]

†*Institute of Geological Sciences, University of Bern, Baltzerstrasse 1+3, 3012 Bern, Switzerland*

‡*The Rossendorf Beamline at the European Synchrotron Radiation Facility (ESRF), Avenue des Martyrs 71, 38043 Grenoble, France*

¶*Institute of Resource Ecology, Bautzner Landstrasse 400, 01328 Dresden*

§*Paul Scherrer Institut, Forschungstrasse 111, 5232 Villingen PSI, Switzerland*

E-mail: georgia.cametti@krist.unibe.ch

Abstract

The structure and thermal stability of a Cd^{2+}-exchanged zeolite with STI framework type was investigated by combining single crystal X-ray diffraction(SCXRD), ab initio molecular dynamic (MD) simulations and X-ray absorption fine structure spectroscopy (XAFS). The room temperature structure was found to be monoclinic, space group F2/m. The Cd^{2+} ions were disordered at partially occupied sites with maximum occupancy of 0.38(2). MD simualtions and XAFS spectroscopy indicated that Cd forms $Cd(H_2O)_6^{2+}$ complexes distributed within the t-sti-1* cage running parallel to [100]. The dehydration was monitored in situ by SCXRD. Upon heating a new contracted phase was observed at 225°C. Compared to the pristine material, the Cd^{2+}-exchanged structure started collapsing already at 325°C, pointing out a reduced thermal stability.

1 Introduction

Cadmium is known to be toxic for human health and environment.[1] Nevertheless, it is largely used in industry as anticorrosive agent, in the fabrication of nickel-cadmium batteries, and as color pigment. Common techniques of cadmium removal from wastewater include filtration, chemical precipitation, coagulation, bioremediation and ion-exchange[2 3 4].[5] Natural zeolites represent a good candidate for use as ionic filter due to their low cost and abundance and extremely efficient Cation Exchange Capacity (CEC). The exchange capacity, together with other well-known properties of zeolitic materials (e.g. selective ion sorption, reversible hydration) is a result of their microporous structure. The latter can be described by a negatively-charged framework constituted by TO_4 tetrahedra (T mainly = Si^{+4} and Al^{3+}) which originates a system of channels and cages which host extraframework cations (EF) and H_2O molecules. The application of zeolites, and of natural ones in particular, in waste-water treatment and in general in environmental remediation processes is well established and has been proved to be extremely effective. Furthermore, Cd-exchanged zeolites, are also highly efficient catalysts[6 7] and have been recently suggested as possible heat-storage media.[8]

In order to properly tune and develop further applications, more information is needed about the framework rigidity and stability of Cd-exchanged zeolites and, since they are usually applied after thermal treatment, particular attention should be paid to eventual phase transitions occurring at high temperatures. Since the properties of these materials are dependent on their porous structure, the understanding of the modifications of the aluminosilicate framework (in terms of pore sizes, channel accessibility, etc.), as a function of EF cations content, plays a key role.

Stellerite is a medium microporous material and represents the Ca-rich member (ideal chemical composition $Ca_8Al_{16}Si_{56}O_{144} \cdot 58\,H_2O$) of natural zeolites with **STI** framework type. The structure can be described by two interconnected channels: one parallel to [001] (2.7 × 5.6 Å) and the other parallel to [100] (4.7 × 5.0 Å) confined by eight- and ten-membered rings of tetrahedra, respectively[9].[10] At room temperature (RT), the structure is orthorhombic

(space group $Fmmm$) and it is referred as phase A.[10] The dehydration occurring upon heating induces the transformation of the room-temperature modification to a new topology known as phase B ($Amma$).[11] This phase is characterized by the statistical rupture (approximately 40%) of one T-O-T connection of the tetrahedral framework. Thus, at high temperature the structure is described by the coexistence of two mutually exclusive topologies. The natural form of stellerite (Ca-STI) does not undergo further structural changes upon heating and at approximately 600 °C turns amorphous.[11] In contrast, the fully Na-exchanged form (Na-STI) is monoclinic $F2/m$ at RT and upon heating different T-O-T connections break leading to the formation of a different B topology ($A2/m$) with respect to the natural one.[12] Moreover, at 525°C, a further contracted phase, known as phase D,[13] forms. Recently, a sample of stellerite exchanged with Ag^+ (Ag-STI) was investigated by X-ray Diffraction and X-ray Absorption Spectroscopy.[14] The results demonstrated that similarly to Na-stellerite the Ag-STI structure at RT is monoclinic and that upon heating it transforms to the same B topology of Na-stellerite (that is not equivalent to the B phase observed in Ca-STI). Interestingly, at 300°C, a new structural configuration, named D', occurs and at 400°C the Ag-STI transforms to the D phase. The structural transformations as a function of temperature for each cationic form of stellerite are summarized in Figure 1.

This study is part of a broader project aimed at investigating the effects, in terms of thermal stability and host-guest interactions, of heavy-metals incorporated into the zeolites structure. The outcomes of this basic research are of paramount importance in several

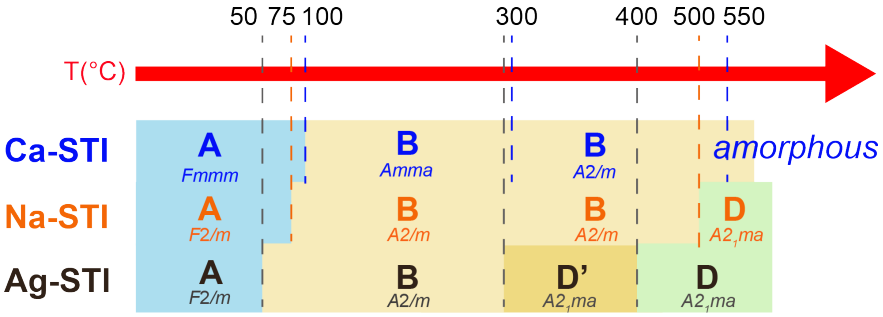

Figure 1: Scheme of the different structural modifications occurring in Ca-,[12] Na-,[12] and Ag-STI[14] as a function of temperature. Corresponding space groups are also reported.

fields, from environmental remediation to industrial applications. Here, we investigated the structure and thermal stability of Cd^{2+}-exchanged stellerite with the aim of i) determining the structural modifications induced by the Cd^{2+} incorporation at RT and ii) tracking the phase transitions occurring as a function of increasing temperature. Structural data were obtained by means of in situ Single Crystal X-ray Diffraction (SCXRD). To get insight into the local arrangement of Cd^{2+} and H_2O within the channels, ab initio Molecular Dynamics (MD) simulations and X-ray Absorption Spectroscopy (XAS) measurements were performed. Finally, we compare our results with those previously reported on other cationic forms of stellerite, in order to draw general conclusions on the effect of transition-metals substitution in **STI** framework-type zeolites.

2 Experimental methods

The sample, a natural stellerite from Giebelsbach, Fiesch, Switzerland, had original chemical composition $Ca_{7.96}K_{0.83}Na_{0.33}(Si_{55.4}Al_{16.42})O_{144}\cdot 58.24\,H_2O$.[15] Natural crystals with dimensions between 0.1 and 1 mm were at first Na-exchanged (same procedure reported in[12]). The Na-stellerite crystals were subsequently placed in a Teflon autoclave filled with 1M $Cd(CH_3COO)_2$ solution (pH = 6) for 4 weeks at 100(2)°C. The cadmium acetate solution was renewed every three days. Afterwards, the crystals were washed with deionized water and their composition was controlled by energy dispersive spectrometry (EDS) using a scanning electron microscope (SEM).

2.1 Single-crystal X-ray Diffraction (SCXRD)

Diffraction data of Cd^{2+}-exchanged stellerite (Cd-STI) were collected on a Bruker APEX II single crystal X-ray diffractometer equipped with MoKα radiation (λ = 0.71073 Å) and a CCD area detector. The crystal (0.150 × 0.200 × 0.100 mm) was glued on the tip of a glass fiber mounted on a goniometer head. To track the dehydration process, data were collected

from 25 to 375°C in steps of 25°C. An in-house build N_2-blower was used. Under these experimental conditions the crystal is exposed to dry atmosphere. Each data collection lasted ca. 8 h and the equilibrium time between the steps was 40 minutes. Data were integrated and corrected for absorption using the Apex 3v.2018.7-2 software package.[16] Structure solutions were performed by Shelxtl-2013.[17] The crystal structure at RT was solved in space group $C2/m$, transformed to $F2/m$ setting according to Quartieri et al. 1987.[18] From 100°C to 250°C the structures were solved in the orthorhombic space group *Amma*.[12] From 275 to 325°C, the structures could only be refined in *Amma* but the maximum resolution drastically dropped (maximum $2\theta = 28.12°$) leading to high R_1 values (see results section for details). From 350 to 375°C only the cell parameters could be extracted. Structural refinements were carried out by SHELXL-2014[19] using neutral atomic scattering factors. The atom coordinates as well as the site labels of the framework atoms were those used in Cametti et al.[12] whereas the extraframework occupants where located from difference Fourier maps.

The rehydration capacity of the crystal heated to 375°C was checked by exposing it to high humidity conditions for 20 days. The structure was measured using the same data-collection strategy applied for the series of high-temperature experiments. To check whether further increase of temperature led to structural collapse, a crystal of Cd-STI was heated ex-situ in air up to 500°C with a heating rate of 20°C/h. The temperature was kept for 2 hours and X-ray data were collected in air at RT. Crystal data, data collection, and refinement details are reported in Table 1. All visualizations of crystal structures were produced by VESTA.[20] Cif files were submitted as supplementary material.

2.2 Molecular Dynamics (MD) Simulations

The MD simulations were performed in NPT (constant temperature and pressure using a flexible cell) ensemble based on the density-functional theory (DFT) using the Gaussian and Plane Waves method (GPW) as implemented in the CP2K simulation package[21].[22] The temperature was controlled at 77°C by a stochastic canonical sampling thermostat.[23] The

Table 1: Crystal data and refinement parameters of Cd-STI at RT, 100, 125, 225, and 275°C.

Crystal data	Cd-STI RT	Cd-STI 100	Cd-STI 125	Cd-STI 225	Cd-STI 275
Crystal size (mm)	0.200 × 0.150 × 0.100	0.200 × 0.150 × 0.100	0.200 × 0.150 × 0.100	0.200 × 0.150 × 0.100	0.200 × 0.150 × 0.100
a-axis (Å)	13.6277(2)	13.6681(2)	13.6214(2)	13.4438(8)	13.2613(14)
b-axis (Å)	18.0966(3)	17.5524(3)	17.4747(3)	17.1244(12)	16.8447(19)
c-axis (Å)	17.6880(3)	17.2739(3)	17.0104(3)	16.3606(12)	16.080(2)
β (°)	90.4250(10)	90	90	90	90
Volume (Å^3)	4362.01(12)	4144.15(12)	4048.98(12)	3766.5(4)	3592.0(7)
Z	1	1	1	1	1
Space group	$F2/m$	$Amma$	$Amma$	$Amma$	$Amma$
Refined chemical formula	$Cd_{7.36}(Si,Al)_{72}O_{144}\cdot 56\,H_2O$	$Cd_{7.10}(Si,Al)_{72}O_{144}\cdot 30\,H_2O$	$Cd_7(Si,Al)_{72}O_{144}\cdot 8\,H_2O$	$Cd_{5.20}(Si,Al)_{72}O_{144}$	$Cd_{4.49}(Si,Al)_{72}O_{144}$
Data collection					
Diffractometer	APEX II SMART	APEX II SMART	APEX II SMART	APEX II SMART	APEX II SMART
X-ray radiation	MoKα $\lambda = 0.71073$ Å	MoKα $\lambda = 0.71073$ Å	MoKα $\lambda = 0.71073$ Å	MoKα $\lambda = 0.71073$ Å	MoKα $\lambda = 0.71073$ Å
X-ray power	50kV, 30 mA	50kV, 30 mA	50kV, 30 mA	50kV, 30 mA	50kV, 30 mA
Monochromator	Graphite	Graphite	Graphite	Graphite	Graphite
Temperature (°C)	RT	100	125	225	275
Time per frame (s)	10	10	10	10	10
Max. 2θ	68.12	61.78	59.14	47.98	28.12
Index ranges	$-21 \le h \le 20$	$-19 \le h \le 18$	$-18 \le h \le 18$	$-15 \le h \le 15$	$-9 \le h \le 9$
	$-25 \le k \le 28$	$-22 \le k \le 25$	$-24 \le k \le 21$	$-19 \le k \le 16$	$-11 \le k \le 11$
	$-27 \le k \le 27$	$-24 \le l \le 24$	$-22 \le l \le 23$	$-18 \le l \le 18$	$-10 \le l \le 10$
No. measured reflections	20744	33995	30860	18528	4663
No. unique reflections	4589	3502	3041	1605	346
No. observed reflections $I \ge 2\sigma(I)$	3850	2769	2311	1003	276
Structure refinement					
No. parameters used in the refinement	207	227	219	195	116
R_{int}	0.0249	0.0473	0.0538	0.1005	0.0690
R_{sigma}	0.0256	0.0305	0.0311	0.0524	0.0286
Goof	1.039	1.078	1.039	1.389	2.203
R_1, $I \ge 2\sigma(I)$	0.0493	0.0556	0.0724	0.1129	0.1514
R_1, all data	0.0598	0.0702	0.0913	0.1571	0.1682
wR^2 (on F^2)	0.1505	0.1635	0.2226	0.3621	0.4107
$\Delta\rho_{min}(-e^{-3})$ close to	-0.96 W3	-1.06 Cd6	-0.84 W3	-0.52 Cd2	-0.51 Cd9A
$\Delta\rho_{max}(e^{-3})$ close to	1.04 W5	1.06 Cd6	0.88 Cd6A	0.70 Cd1	0.72 Cd1

equations of motion were integrated employing 0.5 fs time step. The electron exchange and correlations were described by Perdew-Burke-Erzerhof (PBE) functional.[24] The Kohn–Sham orbitals were expanded using a linear combination of atom-centered Gaussian type orbital functions. In this study a short range double-ζ valence polarized basis set for each atomic kind was used.[25] Dispersion correction was taken into account using the DFT+D2 method.[26]

System set-up. The input structure was obtained starting from the atom coordinates of Ca-stellerite.[12] Ca^{2+} ions were replaced by Cd^{2+} and the number of H_2O molecules was adjusted according to the chemical composition,[15] i.e. seven H_2O for each Cd^{2+}. A fully flexible $2\times1\times1$ supercell was used. The data were collected from a 20 ps long MD trajectory followed by at least 6 ps pre-equilibration. Theoretical Extended X-ray Absorption Fine Structure (EXAFS) spectra were calculated using 50 consequent MD snapshots separated by 100 fs interval. FEFF 8.40 software[27,28] was used to calculate the EXAFS spectra for each Cd^{2+} position in the supercell. In total 16×50 snapshots were averaged to obtain a reference *ab initio* EXAFS spectrum per MD trajectory. The Fermi energies and the scattering potential were calculated self-consistently using the cluster radius of 4 Å. Multiscattering paths up to 4 legs with path lenghts up to 8 Å were taken into account. The Debye-Waller factor was set to 0.0002 $Å^2$. The amplitude reduction factor (S_0^2) was set to 0.9.

2.3 X-ray Absorption Fine Structure Spectroscopy (XAFS)

XAFS spectra were collected at The Rossendorf Beamline at the European Synchrotron Radiation Facility (ESRF, Grenoble). The energy of the X-ray beam was tuned by a double-crystal monochromator operating in channel-cut mode using a Si(111) crystal pair. Two platinum-coated Si mirrors before and after the monochromator were used to collimate the beam into the monochromator and to reject higher harmonics. Cd K-edge (26711 eV) spectra were collected in transmission mode using Ar-filled ionization chambers. Spectra were collected at 15 K using a closed cycle He cryostat (CryoVac). Energy calibration was performed using the zero crossing of the second derivative of the K-edge of metallic Cd (26711

eV) measured simultaneously to the sample scans. Spectra were collected at the Cd K-edge (26711 eV) in transmission mode. Each scan was recorded up to k = 16 $Å^{-1}$ with typical acquisition time of 4 hours. Six scans were averaged to improve the signal-to-noise ratio.

XAFS data reduction and analysis. The data were reduced using the WinXas software.[29] After background subtraction and normalization of the absorption edge jump to unity, the energy was converted to photoelectron kinetic-energy (k-space) by assigning the ionization energy of the Cd K-edge to the first inflection point of the absorption edge. For Extended X-ray Absorption Fine Structure (EXAFS) analyses, a pseudo radial distribution function was obtained by Fourier transforming k^3-χ(k) weighted function between 2.0 and 17 $Å^{-1}$ using a Kaiser-Bessel window function. Structural information was extracted by a multishell fit approach using FEFF8.2[27,28] calculated scattering-paths based on the structure of Ca-STI[12] exchanged with Cd^{2+}. The amplitude reduction factor S_0^2 was fixed to 0.9. A global phase shift ΔE_0 was fitted for all paths.

3 Results

3.1 Structure at room temperature

The SEM-EDS spectra (Figure S1) of the crystals used for the exchanged experiments showed that Na^+ was fully replaced by Cd^{2+}. The incorporation of Cd^{2+} into **STI** framework structure induces a symmetry lowering from orthorhombic *Fmmm* to monoclinic space group *F*2/*m*. The latter corresponds to the space group of Na-[12] and Ag-STI[14] determined at RT. The cell parameters of Cd-STI at room temperature are a = 13.6277(2), b = 18.0966(3), c = 17.6880(3) Å, β = 90.4250(10)°, V = 4362.01(12) $Å^3$. The structure is twinned by pseudomerohedry (matrix [100 010 00-1]), with fractional volume contribution of 0.0573(11). The channels parallel to [100] are more elliptical (5.16×7.66 Å and 5.66×7.30 Å) compared to those of Ca-, Na-[12] and Ag-STI.[14] SCXRD data of the RT structure (Table 2) indicated that Cd^{2+} ions are disordered at partially-occupied sites (maximum occupancy of 0.38)

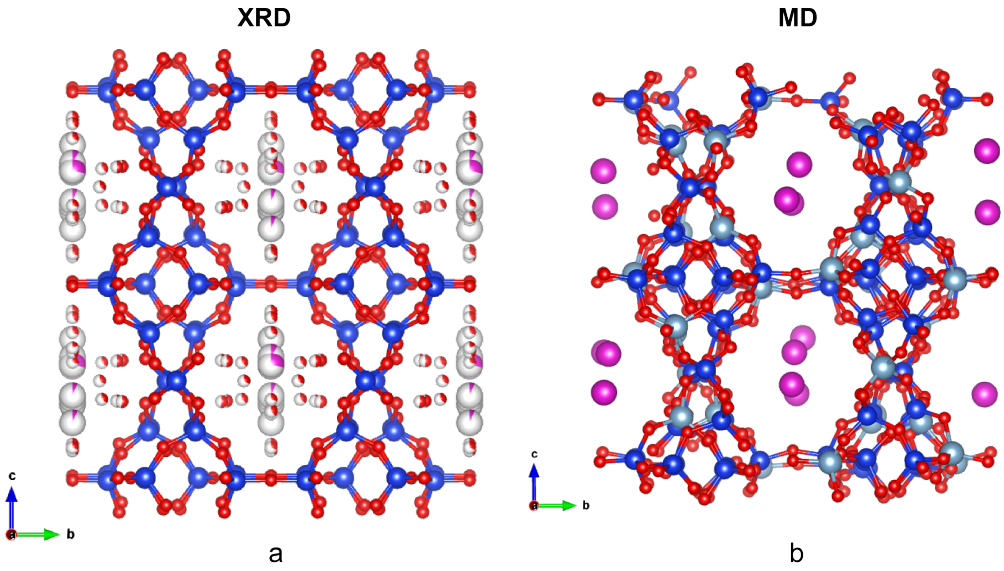

Figure 2: Ball-and-stick representation of Cd-STI structure at RT obtained from X-ray data (a) and MD simulations (b). Cd, O, and Si atoms are displayed as pink, red and blue spheres respectively. Partially colored spheres (a) correspond to partially occupied crystallographic sites. Water molecules are not reported in (b) for sake of clarity. Light blue spheres in (b) represent Al atoms.

distributed in the center of the channels parallel to [100] along the ac plane (Figure 2a). These sites are bonded exclusively to H_2O molecules with distances between 2.269(15) and 2.409(19) Å.

The structural parameters extrapolated from MD trajectories are in agreement with the experimental XRD data. The computed unit-cell parameters deviate from those determined by X-ray of less than 1%, the only exception being the value of the beta angle (Table 3). Figure 2b reports a snapshot of the structure after 16 ps calculations. The distribution of Cd^{2+} varies within the cages and, consistently with X-ray data, Cd ions are mostly located in the center of the ten-membered ring channels surrounded only by H_2O. The average Cd-Ow (Ow being the oxygen of the H_2O molecules) distance is 2.32 Å (Figure 3a) and each Cd^{2+} is surrounded by six H_2O (Figure 3b) arranged in a fairly regular octahedral coordination (Figure 4a), whereas no contacts with the oxygen atoms of the framework are detected. The $Cd(H_2O)_6^{2+}$ complex is distributed within the t-sti-1* cages along the a axis (Figure 4b).

Table 2: Atom coordinates, equivalent displacement parameters, and occupancy of Cd-STI at RT.

Site	Scattering factor	x	y	z	U^{eq} (Å^2)	$Occ.$
T1	Si	0.13682(4)	-0.19433(4)	-0.12259(4)	0.01651(14)	1
T2	Si	0.13645(4)	-0.19009(4)	-0.37066(4)	0.01591(14)	1
T3	Si	-0.05178(4)	-0.41090(3)	-0.25682(4)	0.01609(13)	1
T4	Si	0.13933(4)	-0.31687(3)	-0.25189(4)	0.01494(13)	1
T5	Si	0	-0.23815(6)	-0.5	0.01769(18)	1
O1	O	0.07472(15)	-0.20769(15)	-0.04493(13)	0.0320(5)	1
O2	O	0.06095(15)	-0.18408(13)	-0.44280(13)	0.0313(5)	1
O3	O	0.12514(17)	-0.26440(14)	-0.17966(14)	0.0358(5)	1
O4	O	0.0976(2)	-0.11750(14)	-0.16165(14)	0.0365(5)	1
O5	O	0.12465(16)	-0.27130(13)	-0.33038(13)	0.0322(5)	1
O6	O	0.11515(18)	-0.12324(15)	-0.31289(14)	0.0367(5)	1
O7	O	0.24786(14)	-0.18227(16)	-0.40433(13)	0.0359(5)	1
O8	O	0.06455(15)	-0.38601(13)	-0.24941(19)	0.0395(6)	1
O9	O	-0.0566(2)	-0.5	-0.2556(3)	0.0386(8)	1
O10	O	0.25	-0.35315(15)	-0.25	0.0243(5)	1
Cd1	Cd	0.2854(11)	0	-0.5604(8)	0.0270(14)	0.141(15)
Cd1A	Cd	0.3102(11)	0	-0.5487(5)	0.0313(9)	0.181(8)
Cd1B	Cd	0.2744(17)	0	-0.5462(12)	0.027(3)	0.085(15)
Cd1C	Cd	0.3437(13)	0	-0.5367(6)	0.026(3)	0.048(5)
Cd1D	Cd	0.2361(9)	0	-0.5434(6)	0.0531(14)	0.38(2)
Cd1E	Cd	0.2505(15)	0	-0.5620(14)	0.034(3)	0.086(18)
W1	O	0.2079(12)	-0.1118(8)	-0.5521(8)	0.105(4)	0.5
W1A	O	0.2565(6)	-0.1247(4)	-0.5527(4)	0.061(2)	0.558(17)
W2	O	0.1848(14)	0	-0.0753(6)	0.046(4)	0.44(4)
W3	O	-0.0884(18)	0	-0.5459(16)	0.15	0.49(2)
W4	O	0.2603(13)	0	-0.6796(8)	0.056(5)	0.36(2)
W4A	O	0.3187(15)	0	-0.6709(9)	0.060(6)	0.33(2)
W5	O	0.120(3)	0	-0.623(2)	0.15	0.40(2)
W6	O	0.4612(16)	-0.0695(11)	-0.5384(12)	0.099(6)	0.303(8)
W6A	O	0.407(2)	-0.0870(15)	-0.5624(16)	0.099(8)	0.241(14)
W7	O	0.2266(18)	0	-0.0784(8)	0.057(5)	0.41(4)
W8	O	0.1234(13)	0	-0.0849(10)	0.037(6)	0.209(18)
W9	O	0.179(2)	0	-0.6657(16)	0.114(13)	0.38(3)
W10	O	0	-0.0653(17)	-0.5	0.15	0.42(2)
W11	O	0.388(2)	0	-0.604(2)	0.161(18)	0.41(4)

Table 3: Unit cell parameters of Cd-STI calculated from MD simulations and X-ray data

	MD	**XRD**	**Deviation**(%)
a-axis (Å)	13.52535	13.6277(2)	0.8
b-axis (Å)	18.21387	18.0966(3)	0.6
c-axis (Å)	17.57043	17.6880(3)	0.7
$\alpha(^\circ)$	90.10	90	0.11
$\beta(^\circ)$	93.09	90.4250(10)	3.9
$\gamma(^\circ)$	90.63	90	0.7
Volume (Å^3)	4320.42	4362.01(12)	0.9

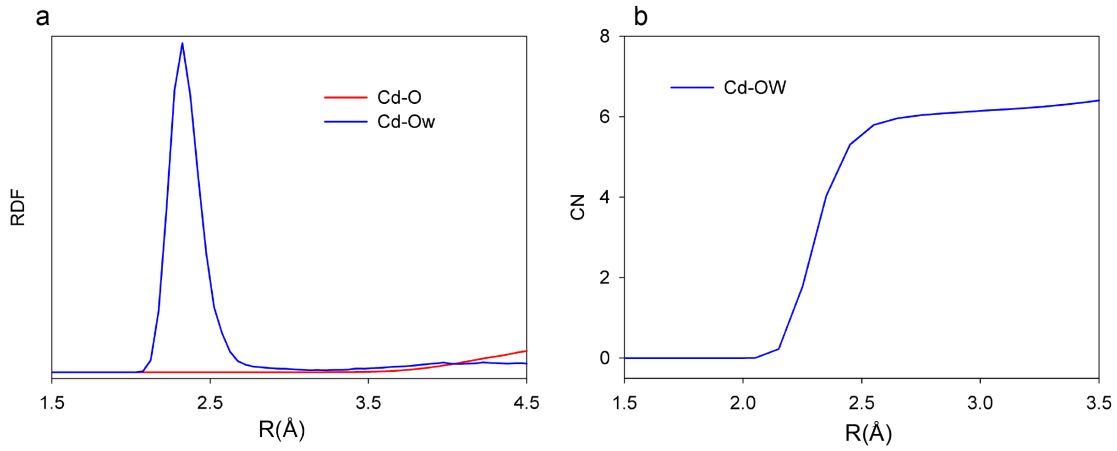

Figure 3: Radial Distribution Function (RDF) (a) and Coordination Number (CN) (b) of Cd-O (O framework oxygen) and Cd-Ow (Ow oxygen of H_2O) calculated from MD trajectories.

The experimental and calculated k^3-χ(k) weighted function and the corresponding Fourier Transform (uncorrected for shift) of Cd-STI are reported in Figure 5. The FT shows mainly two peaks at 1.8 and 3.16 Å. The first peak can be fitted by a Cd-O shell with corresponding Cd-O distance R = 2.28 Å and coordination number CN = 6.3. To correctly interpret the second peak at 3.16 Å, the spectrum was FT backtransformed in the range between 2.5 and 3.6 Å. The result clearly indicated the contribution of a heavy element that, in our case can only be ascribed to Cd. Thus, a second shell Cd-Cd was inserted in the refinement. The final structural parameters obtained from the EXAFS refinement are reported in Table 4.

The local configuration of Cd^{2+} ions surrounded by six H_2O is in agreement with both experimental (SCXRD data) and theoretical (MD simulations) results which indicated that in fully hydrated Cd-STI, Cd^{2+} ions do not bond to the framework oxygen but are only

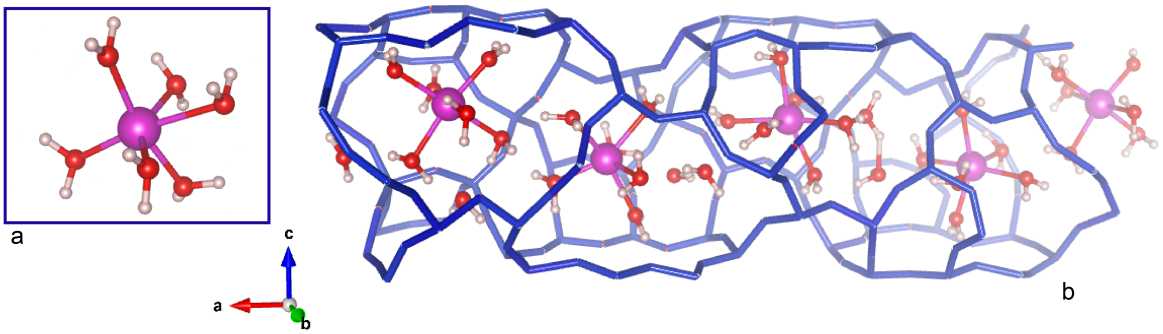

Figure 4: Fragment of Cd-STI structure obtained from MD trajectories. The framework is represented by blue sticks obtained by T-O-T connections. Six-fold coordination of Cd^{2+} with H_2O (a) and distribution of $Cd(H_2O)_6^{2+}$ complexes (b) within the t-sti-1* cages.

Table 4: Structural parameters of Cd-STI at 15K determined from EXAFS analysis

Shell	CN ±25%	R(Å) ±0.002	σ^2(Å^2) ±0.002	ΔE_0 (V)
Cd-O	6.3	2.28	0.0050	7.56
Cd-Cd	0.6	3.46	0.0047	7.56

surrounded by H_2O. However, this structural configuration cannot explain Cd-Cd distances at 3.46 Å. The latter are instead typical of $Cd(OH)_2$ with brucite-type structure[30].[31] Cd-hydroxide can precipitate under the experimental conditions used for the exchange experiments (ph =6 and T = 100°C). As a confirmation, SEM-EDS pictures of the powder used for XAFS experiments revealed the presence of small particles rich in Cd (Figure S2). It is worth noting that an attempt to identify this additional phase by X-ray powder diffraction was not successful, mainly due to the low amount and small dimension ($< 1\mu$m) of the crystallites.

Although the average <Cd-Ow> distances obtained by the different methods (X-ray diffraction, simulations and X-ray spectroscopy) are consistent with each other, discrepancies are visible when comparing the χ(k) function calculated from MD trajectories and the one obtained by EXAFS measurements. The theoretical χ(k) is shifted toward low k values compared to the experimental one (Figure S4). Such shift is reflected in the higher <Cd-Ow> distance (2.32 Å) extrapolated by the Md trajectories with respect to that obtained by the fitting of the EXAFS data (2.28 Å). The tiny amount of an additional phase found in the

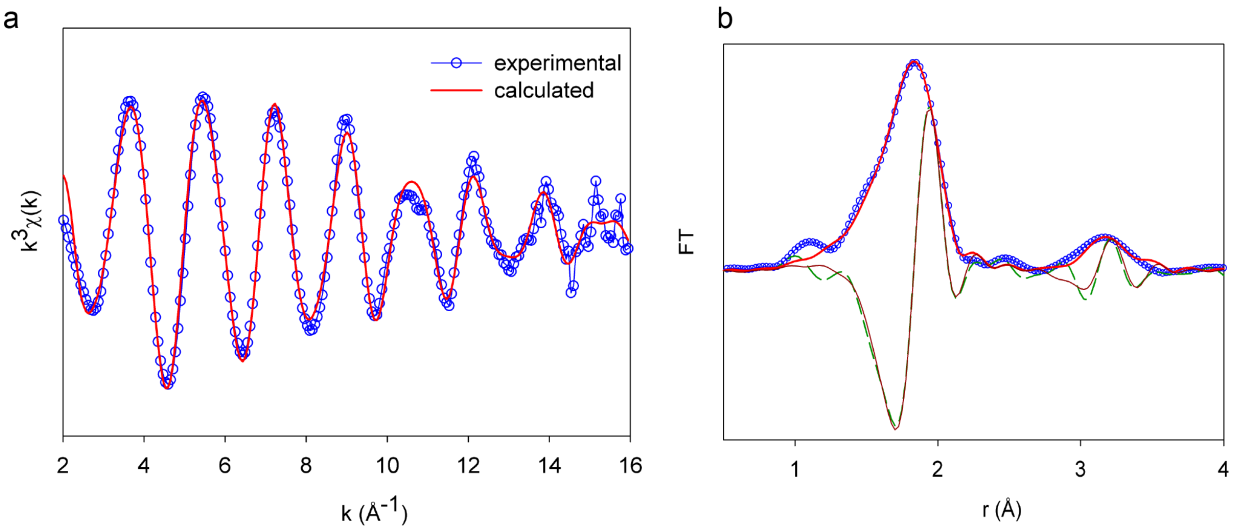

Figure 5: (a) k^3-χ(k) weighted function and (b) Fourier transformed EXAFS spectra(uncorrected shift) of Cd-STI at 15 K (-258°C). Blue circles and red lines represent the experimental data and corresponding fits, respectively. Measured (dashed line) and fitted (continuous line) imaginary parts of FT are also displayed.

powder used for the XAS experiments cannot justify the reported discrepancy. Thus, other factors should be taken into account. Shorter Cd-Ow distances can arise as a consequence of a reduced hydration shell. For testing purposes, we performed a geometry optimization of the Cd-STI structure obtained from MD by removing one H_2O from the coordination shell of Cd^{2+}, i.e. hypothesizing six H_2O per Cd^{2+} ion. The average Cd-Ow decreased to 2.26 Å indicating that a system with less than seven H_2O per Cd^{2+} would match the experimental one. With this regard, we have to consider that XAFS experiments were conducted under dry conditions. Hence, part of the H_2O could be lost by the zeolite, leading to a slightly less-hydrated system compared to that assumed in MD simulations.

3.2 Structural changes upon heating

The dehydration of Cd-STI starts at 50°C, in correspondence of the decrease of the unit-cell volume from 4362.01(12) to 4352.62(12) $Å^3$ (Figure 6; Figure 7a).

At 100°C the space group changes from monoclinic $F2/m$ to orthorhombic $Amma$. This

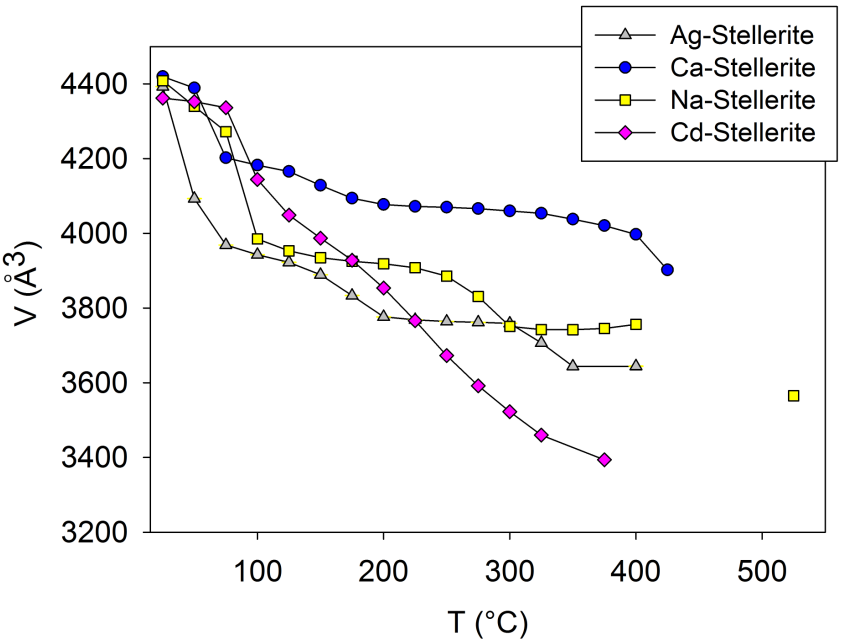

Figure 6: Unit-cell volume trend of Cd-STI (pink diamonds) as a function of temperature determined by SCXRD. Corresponding values of Ca-,[12] Na-[12] and Ag-STI[14] are also reported for comparison.

change is accompanied by the gradual decrease of the beta angle from RT ($\beta = 90.4250(10)°$) to 125°C ($\beta = 90.01°$). To assign the proper space group, test refinements of the data sets collected at 100 and 125°C were also performed in the monoclinic space group $A2/m$.[12] No significant differences were observed between the results achieved in $Amma$ and $A2/m$ and as a consequence the orthorhombic space group was preferred.

At 100°C, 5% of (Si,Al) at T1P site move toward a new position (T1PD), indicating the onset of the rupture of the T4-O3P-T1P connection (Table S1, Figure 7b). At 125°C the percentage of new T1PD sites increases to 20% and the new connection T1PD-OD-T1PD forms within the channels parallel to [100] (Table S2, Figure 7c). Thus, the structure transforms to the B topology[12] also reported for Ca-STI. In addition, 20% of the T4 sites moves toward two new positions (T4D and T4DA) and 5% of (Si,Al) at T1 migrate to T1D. Note, that the occurrence of this additional site was observed in Ca-STI only at 400°C.[12] Upon further heating, the percentage of broken connections increases. This process is accompanied by strong disorder and at 150°C an additional site (T4DB), close to T4

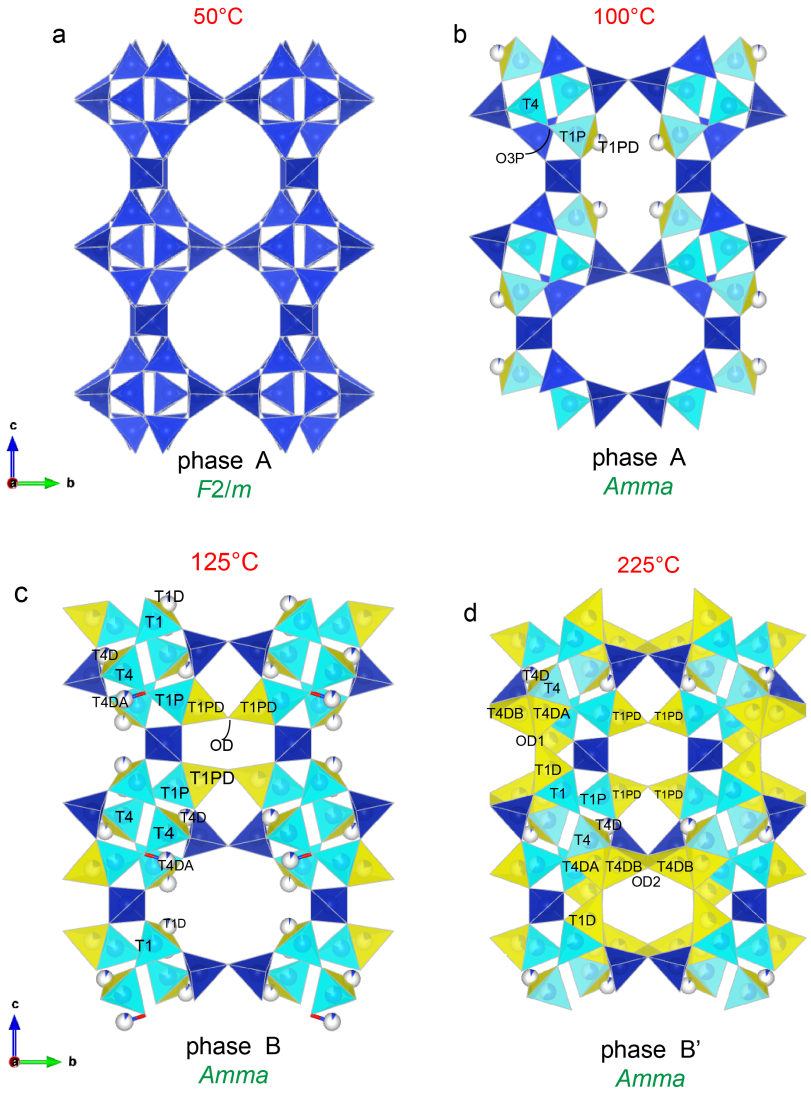

Figure 7: Polyhedral representation of the crystal structure of Cd-STI at 50 (a), 100 (b), 125 (c), and 225°C (d). The blue tetrahedra represent the (Si,Al)O_4 units. The tetrahedra involved in the rupture process are displayed in cyan and the new ones, forming as a consequence of the migration of the original T sites, in yellow.

and refined with Si scattering factor, was inserted in the refinement. At 225°C, two new connections were observed: T4DB-OD2-T4DB (which does not occur in Ca-STI[12]) and T4DA-OD1-T1D (which corresponds to T4D-OD1-T2D in Ca-STI) (Table S3, Figure 7d). The formation of the new tetrahedra T4DB induces a further closure of the channels along [100]. We refer to this structural configuration as B' to distinguish it from B. At this temperature the occupancies of the new T sites converge to 0.403(4), 0.318(5), and 0.159(2)

for T1PD, T1D, and T4DB (= T4DA) respectively.

At 275 °C the number (4463 total and 346 unique) and quality of measured reflections drastically decreased (Table 1). An attempt to refine the structure in $Amma$, despite the poor agreement factors and the low value of the observed/parameters ratio (Table 1), indicated that the Cd-STI preserves the B' configuration. For comparison, test refinements were also carried out in $A2_1ma$ space group using as starting coordinates of the framework atoms those of the D phase of Ag-STI:[14]however, in this case it was impossible to obtain a reliable model. The same procedure, applied to the data set collected at 300°C, led to similar conclusions, suggesting that the structure does not further change at least up to this temperature. From 325 to 375°C, the reflections split and broaden and the total number of measured data further decreases (Figure S3), due to the onset of the structural collapse. In this temperature range only the cell parameters could be determined. The total-unit cell volume contraction determined at 375°C is 22% of that measured at RT.

During the dehydration process the disorder of Cd ions becomes considerably more pronounced and on average, from 100°C on, Cd distributes over several sites with occupancy lower than 10% (Tables S1-S3). For this reason, not all cadmium ions could be located in the structural refinements (Table 1) and the refined number of Cd atoms per formula unit in all data sets is lower than 8.

The crystal heated at 375°C was used for the rehydration experiment. The maximum achievable resolution was $2\theta = 29.02°$ and the number of unique reflections was only 359 making it impossible to solve the structure. An attempt to refine the data set with the model used for the one measured at 275°C was not satisfactory and as a consequence only the cell-parameters could be determined. The unit-cell volume (3398.4(9) Å^3) is close to that of the structure dehydrated at 375°C, indicating that no H_2O could be reabsorbed. In contrast, no reflections were detected in the sample used for the ex-situ experiment performed at 500°C, showing that at this temperature Cd-STI turns amorphous.

4 Discussion

The main effect of Cd^{2+} incorporation into stellerite at RT is the distortion of the framework from orthorhombic to monoclinic. The same distortion was observed in Na[12]-, although less pronounced, and in Ag-STI.[14] In Ag-STI such distortion was ascribed to the distinct electronic configuration of Ag^{+} with respect to Na^{1} that results in different electrostatic interactions with the oxygen atoms of the framework. XAFS data and MD calculations unambiguously showed that in the RT phase of Cd-STI Cd^{2+} ions only bond to H_2O molecules, forming $Cd(H_2O)_6^{2+}$ complexes within the t-sti-1* cages. Hence, the strain of the aluminosilicate framework in Cd-STI is exerted indirectly through hydrogen bonds between H_2O and the framework oxygen. A similar configuration is observed in Ca-STI, where Ca^{2+} ions bond uniquely to H_2O molecules. To better compare the local environment in Cd- and Ca-STI, MD simulations of the Ca-STI structure were also performed. In Figure 8 is reported a snapshot of the calculated Cd-STI and Ca-STI structures showing the t-sti-1* cage: the different ionic radius of Cd^{2+} (0.95 Å) and Ca^{2+} (1.0 Å) results in a different coordination (calcium is coordinated by seven H_2O (Figure S5)) and, as a consequence, in a different hydrogen-bonds network which directly affects the strain on the framework.

The trend of the unit-cell volume of Cd-STI as a function of temperature, as well as the corresponding structural changes, follows that of Ca-STI up to approximately 100°C. However, from this temperature on, it changes significantly: the curve becomes much steeper and the final volume contraction at 375°C is approximately twice as that of Ca-STI (Figure 6). Differently to the pristine material, the Cd-form transforms to orthorhombic at 100°C and never turns monoclinic with the increase of temperature. Moreover, from 100°C on, the dehydration-process is much faster and the structural transformations are shifted toward lower temperatures. Thus, although the Cd-exchanged structure transforms to the B topology observed in Ca-STI, this transformation (associated with the formation of the new connection within the ten-membered ring channels) occurs at lower temperatures (125°C in Cd-STI and 175°C in Ca-STI). It should be stressed that the shift of the whole process toward

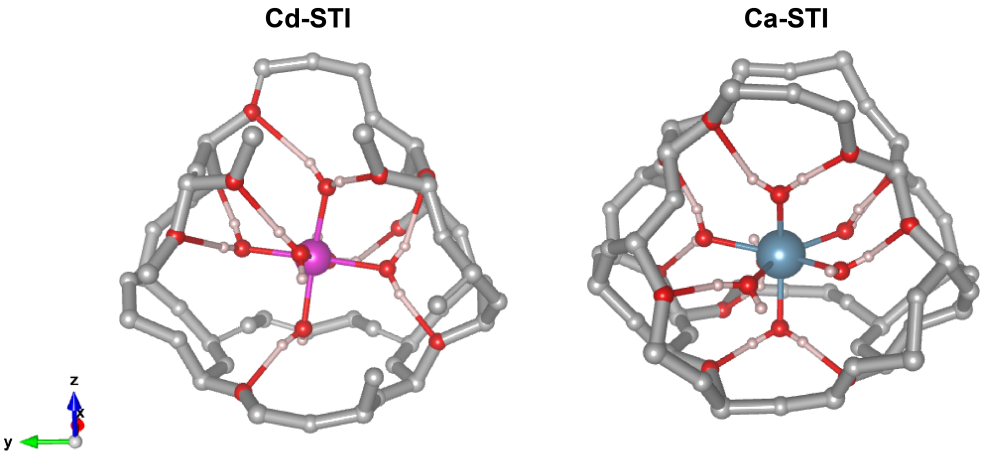

Figure 8: Detail of the t-sti-1* cage of the Cd-STI and Ca-STI structures obtained from MD simulations. The framework is reported in grey, Cd and Ca atoms in pink and light-blue respectively. Red spheres represent oxygen of the H_2O and oxygen of the framework involved in hydrogen bonds. Hydrogen atoms are displayed as light-pink spheres.

lower temperature does not amount only to 100°C, but becomes progressively wider (e.g. the unit-cell volume of Cd-STI at 175°C V = 3928.02(18) Å^3 is comparable to that of Ca-STI measured at 400°C V = 3902 Å^3). Moreover, the B topology further modifies at 225°C when the connections T4DA-OD1-T1D and T4DB-OD2-T4DB form. This additional structural change arises from the migration of the T4 sites toward T4DA and T4DB positions. As reported before the T4DA-OD1-T1D connection corresponds to the T4D-OD2-T2D one in Ca-STI (please note that the sites have a different labeling due different space group, i.e. *Amma* for Cd-STI and $A2/m$ for Ca-STI) whereas the T4B-OD2-T4B link does not form in natural stellerite. This new link resembles the one which forms in Na- and Ag-STI (at 400°C and 500°C, respectively) when the structures transform to the contracted D phase. If we compare the B' topology observed in this study with the D one reported for Na- and Ag-STI (Figure 9) the similarities are quite evident (the equivalent tetrahedra are displayed in red). The main distinction is that the B' phase is not ordered, i.e. two mutually exclusive configurations (with the percentage corresponding to the occupancy of the T sites involved in the breaking process) coexist in the structure; in contrast, the D phase is an ordered modification where 50% of the new positions (yellow tetrahedra in Figure 9) and 50% of the original ones

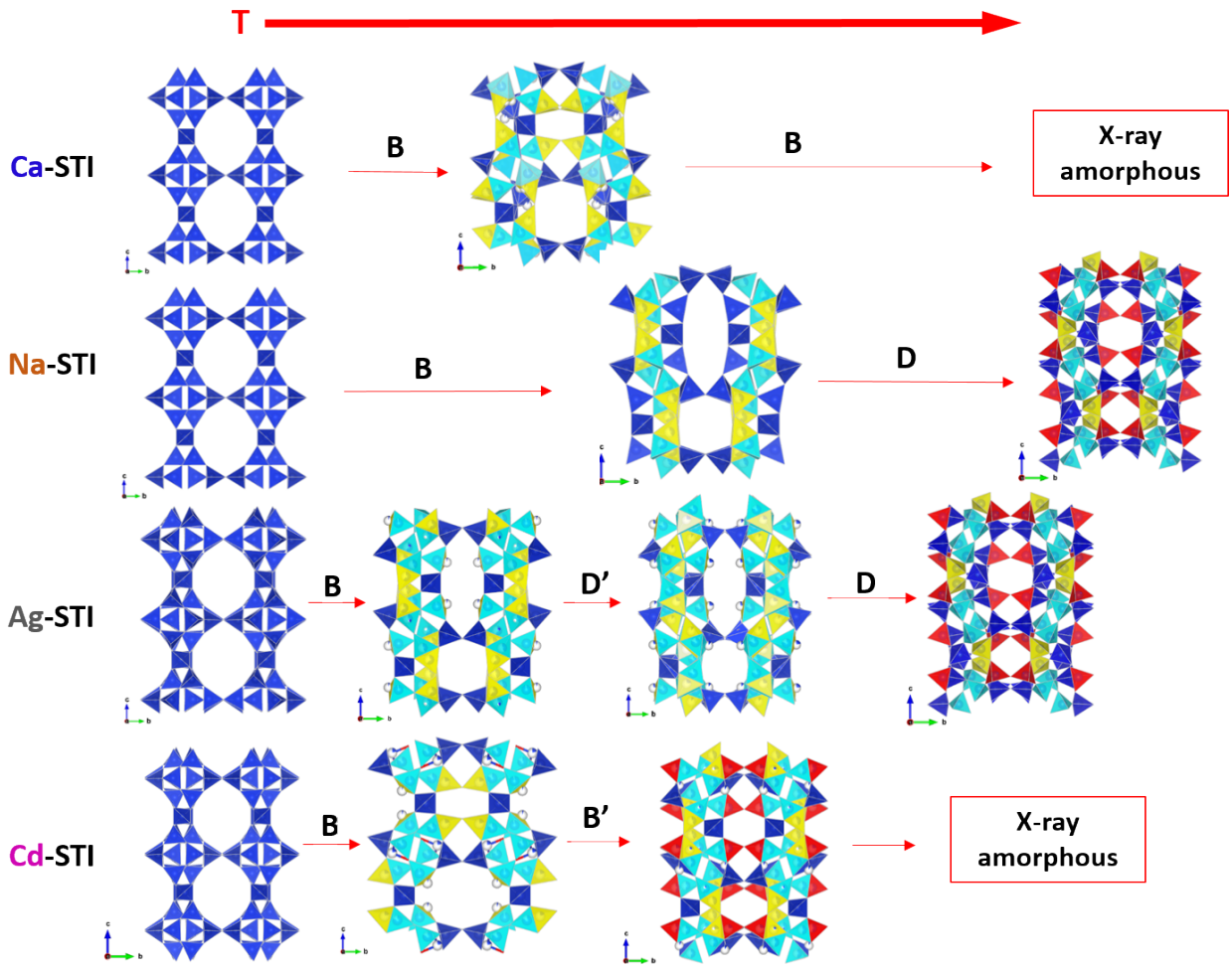

Figure 9: Summary of the main structural modifications of Ca-,[12] Na-,[12] Ag–,[14] and Cd-STI (this study) which occur as a function of temperature. Color code as reported in Figure 7. Equivalent connections in B' and D phases are represented by the red tetrahedra.

(cyan tetrahaedra) are fully occupied. Such difference is also reflected in the space group of the two structures, e.g. $A2_1ma$ (D phase of Ag-STI) and $Amma$ (B' phase of Cd-STI). Thus, even if the dehydration behavior could be related to that of Ca-STI (transformation to B phase followed by subsequent amorphization), the path and the structural rearrangements are actually different. Most important, the diffraction experiments demonstrated that the structure of the Cd-STI starts collapsing already at 325°C (Figure S3) indicating that its thermal stability is significantly lower compared to that of the Ca-form. With this regard, it must be pointed out that the results presented in this study were obtained by using the same

experimental set-up applied in the investigation of the thermal stability of Ca-, Na-[12] and Ag-STI.[14] As a consequence, we can exclude any influence of the experimental conditions (e.g. heating system, heating rate, humidity) in the observed differences and ascribe the structural changes only to the EF species.

The reduced thermal stability of the Cd-form compared to that of the Ca one can be explained considering two aspects: i) as we previously pointed out, Cd^{2+} is initially coordinated only to six water molecules. Hence, compare to Ca-STI the non-bonded water is released more easily; ii) the framework of Cd-STI is more contracted, in terms of channels dimension, and even more distorted (if the deviation from the orthorhombic symmetry is considered) than the Ca-STI. The initial degree of distortion, dictated not only by the size but also by the bonds directionality of the EF cations, has an effect on the dehydration path, i.e. the higher the contraction at RT, the less the thermal stability.

5 Conclusions

In this study we investigated the crystal structure and the thermal stability of Cd^{2+}-exchanged stellerite by combining a theoretical and experimental approach. The Cd-STI structure at RT was found to be monoclinic, $F2/m$. The main structural transformations occurring upon dehydration can be summarized as follow: i) transformation to the B topology at 125°C (equivalent to the one observed in Ca-STI); ii) transformation, at 225°C, to a highly contracted phase B' still characterized by the system of mutually exclusive face-sharing tetrahedra; iii) amorphization of the structure (T= 500°C).

When compared to the other known exchanged-forms of stellerite, the Cd-STI is the one which, in the investigated temperature range, contracts more. From an application point of view, the main important outcome is that the structure starts collapsing already at 325°C, meaning that the EF occupant has a huge impact on the thermal stability of the new-produced material.

If the structures of the known exchanged-forms of stellerite as a function of temperature are compared (Figure 9), two main conclusions can be drawn:

i) The valence of the extraframework cation seems to affect the structural topology which forms upon heating. The B topologies of Cd- and Ca-STI are equivalent to each other, as well as those of Na- and Ag-STI. A possible explanation is the number of the EF cations per formula unit: the divalent cations are always one half with respect to the monovalent ones (e.g. 8 Ca versus 16 Na per formula unit). Hence, at the beginning of the dehydration process when the T-O-T connections start breaking, the position of the new T sites is influenced by the available space within the cages: in the structures containing the divalent-cations (Cd- and Ca-STI) the new T sites can flip in the center of the ten-membered ring channels (Figure 9). A corresponding T-O-T connection does not form in Na- and Ag-STI where, the initial position and distribution of the EF cations (which bond to both framework oxygen atoms and H_2O molecules) preclude the migration of the T sites to the center of the channels. Only at higher temperatures when the EF cations approach the walls of the zeolitic channels, the additional link (reported in red in Figure 9) can form.

ii) The transition metals have an impact on the degree of the framework distortion and, as a consequence on the response of the structure to the heating stimuli. The monoclinic structure of Na-STI slightly deviates (beta angle and channel dimensions) from the orthorhombic symmetry whereas in both Ag- and Cd-STI the monoclinic distortion at RT is much more obvious. In view of our findings, the initial degree of straining exerted by the EF cations is also responsible for the dehydration path: in both Ag- and Cd-STI the structural rearrangements induced by heating occur at lower temperature compare to Na- and Ca-STI, suggesting that the more the distortion at RT the faster the dehydration process.

Supporting Information Available

The following files are available free of charge.

- Supplementary material: Details on the strategy used to refine SCXRD data; SEM-EDS spectrum of Cd-stellerite sample used for SCXRD experiments; SEM-EDS spectrum of Cd-stellerite powder used for XAFS experiments; reconstructed precession images of of $h0l$ and $0kl$ layers of Cd-stellerite structure at 275, 300, 325, and 375°C; Experimental and calculated k^3-weighted $\chi(k)$ function obtained from EXAFS and MD simulations; Radial distribution function (RDF) of Ca-Ow obtained from MD trajectories; Atom coordinates, equivalent displacement parameters, and occupancy of Cd-STI at 100, 125, and 225°C. (PDF)

- Crystallographic data of Cd-STI RT (CIF)

- Crystallographic data of Cd-STI 100°C (CIF)

- Crystallographic data of Cd-STI 125°C (CIF)

- Crystallographic data of Cd-STI 225°C (CIF)

Author Information

Corresponding Author

*E-mail: georgia.cametti@krist.unibe.ch Phone +41 316315248

ORCID

Georgia Cametti: 0000-0002-31863074 Andreas C. Scheinost: 0000-0002-6608-5428 Sergey V. Churakov: 0000-0001-8213-9206

Author Contributions

G.C. conceived the research, performed the experiments, analyzed the data, and wrote the manuscript. A.C.S. analyzed the XAFS data, S.V.C set up and analyzed the MD simulations. The mansucript was written through the contributions from all authors. All authors have given approval to the final version of the mansucript.

Funding

This study benefits from funding awarded to G.C. by the Swiss National Science Foundation (SNF): Ambizione grant no PZ00P2 173997.

Acknowledgement

We acknowledge access to the Swiss National Supercomputing Center (CSCS) and UBELIX HPC cluster at the University of Bern. We are thankful to Thomas Armbruster for reading the manuscript and to Giuseppe A. Zito for his help in preparing Matlab script.

References

(1) Godt, J.; Scheidig, F.; Grosse-Siestrup, C.; Esche, V.; Brandeburg, P.; Reich, A.; Groneberg, D. A. The toxicity of cadmium and resulting hazards for human health. *J. Occup. Med. Toxicol.* **2006**, *doi:10.1186/1745-6673-1-22*.

(2) Charerntanyarak, L. Heavy metals removal by chemical coagulation and precipitation. *Water Sci. Technol.* **1999**, *39*, 135–138.

(3) Carolin, C. F.; Kumar, P. S.; Saravanan, A.; Joshiba, G. J.; Naushad, M. Efficient techniques for the removal of toxic heavy metals from aquatic environment: a review. *J. Environ. Chem. Eng.* **2017**, *5*, 2782–2799.

(4) Rodriguez-Narvaez, O. M.; Peralta-Hernandez, J. M.; Goonetilleke, A.; Bandala, E. R. Treatment technologies for emerging contaminants in water: a review. *Chem. Eng.J.* **2017**, *323*, 361–380.

(5) Pyrzynska, K. Removal of cadmium from wastewaters with low-cost adsorbents. *J. Environ. Chem. Eng.* **2019**, *7*, 2213–3437.

(6) Onyestya, G.; Kallo, D. Hydration of acetylene on Zn- and Cd-zeolites. *Micropor. Mesopor. Mat.* **2003**, *61*, 199–204.

(7) Zhang, Y.; Qu, Y.; Wang, D.; Zeng, X. C.; Wang, J. Cadmium modified HZSM-5: a highly efficient catalyst for selective transformation of methanol to aromatics. *Ind. Eng. Chem. Res.* **2017**, *56*, 12508–12519.

(8) Aprea, P.; de Gennaro, B.; Gargiulo, N.; Peluso, A.; Liguori, B.; Iucolano, F.; Caputo, D. Sr-, Zn- and Cd-exchanged zeolitic materials as water vapor adsorbents for thermal energy storage applications. *Appl. Therm. Eng.* **2016**, *106*, 1217–1224.

(9) Baerlocher, C.; Meier, W. M.; Olson, D. H. *Atlas of Zeolite Framework Types, Structure Comission of the IZA*; Elsevier, 2001.

(10) Galli, E.; Alberti, A. The crystal structure of stellerite. *B. Soc. Fr. Mineral. Cr.* **1975**, *98*, 11–18.

(11) Arletti, R.; Mazzucato, E.; Vezzalini, G. Influence of dehydration kinetics on T-O-T bridge breaking in zeolites with framework type STI: The case of stellerite. *Am. Mineral.* **2006**, *91*, 628–634.

(12) Cametti, G.; Fisch, M.; Armbruster, T. Thermal behavior of stilbite and stellerite revisited and dehydration of their Na-exchanged forms: Considerations on the memory effect of the STI framework type. *Micropor. Mesopor. Mat.* **2017**, *253*, 239–250.

(13) Sacerdoti, M. The crystal structure of zeolite barrerite dehydrated in air at 400-450°C. *Micropor. Mesopor. Mat.* **2007**, *102*, 299–303.

(14) Cametti, G.; Scheinost, A. C.; Giordani, M.; Churakov, S. V. Framework modifications and dehydration path of a Ag+-modified zeolite with STI framework type. *J. Phys. Chem. C* **2019**, *123*, 13651–13663.

(15) Armbruster, T.; Kohler, T.; Meisel, T.; Nägler, T. F.; Götzinger, M. A.; Stadler, H. A. The zeolite, fluorite, quartz assemblage of the fissures at Gibelsbach, Fiesch (Valais, Switzerland): crystal chemistry, REE patterns and genetic speculations. *Mineral. Petrogr. Mitt.* **1996**, *76*, 131–146.

(16) Bruker, AXS APEX3 v2018.7-2.

(17) Sheldrick, G. M. A short history of SHELX. *Acta Crystallogr. A* **2008**, *64*, 112–122.

(18) Quartieri, S.; Vezzalini, G. Crystal chemistry of stilbites: structure refinements of one normal and four chemically anomalous samples. *Zeolites* **1987**, *7*, 163–170.

(19) Sheldrick, G. M. Crystal structure refinement with SHELXL. *Acta Crystallogr. C* **2015**, *71*, 3–8.

(20) Momma, F., K.; Izumi VESTA 3 for three-dimensional visualization of crystal, volumetric and morphology data. *J. Appl. Crystallogr.* **2011**, *44*, 1272–1276.

(21) VandeVondele, J.; Krack, M.; Mohamed, F.; Parrinello, M.; Chassaing, T.; Hutter, J. Quickstep: Fast and accurate density functional calculations using a mixed Gaussian and plane waves approach. *Comput. Phys. Comm.* **2005**, *167*, 103–128.

(22) www.cp2k.org.

(23) Bussi, G.; Donadio, D.; Parrinello, M. Canonical sampling through velocity rescaling. *J. Chem. Phys.* **2007**, *126*, 014101.

(24) Perdew, J.; Burke, K.; Ernzerhof, M. Generalized gradient approximation made simple. *Phys. Rev. Lett.* **1996**, *77*, 3865–3868.

(25) VandeVondele, J.; Hutter, J. Gaussian basis sets for accurate calculations on molecular systems in gas and condensed phases. *J. Chem. Phys.* **2007**, *127*, 114105.

(26) Grimme, S. Semiempirical GGA-type density functional constructed with a long-range dispersion correction. *J. Comput. Chem.* **2006**, *27*, 1787–1799.

(27) Ankudinov, A. L.; Ravel, B.; Rehr, J. J.; Conradson, S. D. Real-space multiple-scattering calculation and interpretation of X-ray-absorption near-edge structure. *Phys. Rev. B* **1998**, *58*, 7565–7576.

(28) Ankudinov, A. L.; Rehr, J. J. Theory of solid-state contributions to the X-ray elastic scattering amplitude. *Phys. Rev. B* **2000**, *62*, 2437–2445.

(29) Ressel, T. A program for X-ray absorption spectroscopy data analysis under MS-windows. *J. Synchrotron Radiat.* **1998**, *5*, 118–122.

(30) Hemmingsen, L.; Bauer, R.; Bjerrum, M. J.; Schwarz, K.; Blaha, P.; Andersen, P. Structure, chemical bonding and nuclear quadrupole interactions of beta-($Cd(OH)_2$): Experiment and first principles calculations. *Inorg. Chem.* **1999**, *38*, 2860–2867.

(31) Gräfe, M.; Singh, B.; Balasubramanian, M. Surface speciation of Cd(II) and Pb(II) on kaolinite by XAFS spectroscopy. *J. Colloid. Interf. Sci.* **2007**, *315*, 21–32.